Optimization of NEMS pressure sensors with a multilayered diaphragm using silicon nanowires as piezoresistive sensing elements

Optimization of NEMS pressure sensors with a multilayered diaphragm using silicon nanowires as piezoresistive sensing elements

Liang Lou[1,2]**, Songsong Zhang**[1]**, Woo-Tae Park**[3]**, J M Tsai**[2]**, Dim-Lee Kwong**[2] **and Chengkuo Lee**[1]

[1] Department of Electrical and Computer Engineering, National University of Singapore, 4 Engineering Drive 3, Singapore 117576

[2] Institute of Microelectronics, Agency for Science, Technology and Research, 11 Science Park Road, Singapore 117685

[3] Department of Mechanical and Automotive Engineering, Seoul National University of Science and Technology, Seoul, Korea

E-mail: elelc@nus.edu.sg and wtpark@seoultech.ac.kr

Abstract

A pressure sensor with a 200 μm diaphragm using silicon nanowires (SiNWs) as a piezoresistive sensing element is developed and optimized. The SiNWs are embedded in a multilayered diaphragm structure comprising silicon nitride (SiN_x) and silicon oxide (SiO_2). Optimizations were performed on both SiNWs and the diaphragm structure. The diaphragm with a 1.2 μm SiN_x layer is considered to be an optimized design in terms of small initial central deflection (0.1 μm), relatively high sensitivity (0.6% psi^{-1}) and good linearity within our measurement range.

(Some figures may appear in colour only in the online journal)

1. Introduction

Piezoresistive transduction, which is one of the earliest demonstrations of mechanisms suitable for microdevices, has been widely used in microelectromechanical system (MEMS) sensors since the first report by Smith [1, 2]. Micromachined piezoresistive sensors are the most widely used microsensors in industry today, partially due to the relatively straightforward interface circuitry and the ease of process integration. Other than the well-known automotive applications for pressure sensors including engine manifold monitoring, tire pressure monitoring and both oil and brake fluid pressures [3–7], pressure is also one of the most important physical parameters for various biomedical application such as measuring intrauterine pressure during birth, monitoring the inlet and outlet pressures of blood in kidney dialysis and the cardiovascular system, measuring and controlling the vacuum level used to remove fluid from the eye during eye surgery [8–11]. One of the earliest research efforts in biomedical applications is a pressure sensor developed by Samaun *et al* for biomedical instrumentation applications including cardiovascular catheterization [12]. A 50 μm thick silicon substrate was used to fabricate a single-crystal silicon diaphragm of 1.2 mm in diameter and 5 μm in thickness, where the diaphragm with four integrated piezoresistors made by a diffusion process was released using the anisotropic wet etching technique. They also developed a technique to define precisely the thickness of the membrane within a 1 μm thickness, while the size of diaphragm could be reduced to as small as 0.8 mm. Another milestone in pressure sensor development was the merging of a sensor and its interface circuitry on a monolithically fabricated die. This was first implemented by Borky and Wise in 1980 with their development of a micromachined piezoresistive pressure sensor integrated into a triple-diffused bipolar circuit process [13].

On the other hand, minimally invasive surgical procedures are preferred because of small incisions, i.e. leaving small tissue scar after healing. The merits of such surgical procedures include a shorter hospitalization period and quick recovery from incision trauma. For many cardiovascular and thoracic interventional procedures, passing a guidewire through a vascular vessel is the first step followed by surgical procedures such as stenting. The success rate of treating a vascular lesion via endovascular methods (wires, catheters and angioplasty balloons) depends mainly on how a guidewire passes across the lesion successfully. Passage of the guidewire is primarily through the haptic feeling of the surgeon; thus the force or pressure feedback of the passing guidewire is extremely difficult to quantify. Besides, quantitative information of force or pressure feedback of the passing guidewire can be used in facilitating robotic surgeries [14, 15]. MEMS technology has enabled guidewires to be sensorized by integrating pressure sensors into it [16–19]. In view of such advantage, a further downsizing effort in making pressure sensors will enable a compact and sophisticated sensorized guidewires. For example, based on a polysilicon surface micromachining process, a piezoresistive pressure sensor using a polysilicon diaphragm area of $103 \times 103~\mu m^2$ has been fabricated by E Kalvesten *et al* for clinical blood pressure measurements with a sensitivity of $2.0~\mu V~V^{-1}~mmHg^{-1}$, resulting in a pressure measurement accuracy of more than 2 mmHg for balloon angioplasty applications [15].

In the oil well down-hole digger head which operates in a harsh environment of 300 °C or above, pressure monitoring is also one of the functions to be carried out [20]. The fiber-optics-based Fabry–Perot interferometer and a fiber Bragg grating-based pressure sensor system have been the mainstream approach [21]. Using MEMS-based piezoresistive sensors for the oil well down-hole application in high temperature environment demands stable piezoresistive materials, e.g. single crystal silicon.

By leveraging the advanced semiconductor process technology, CMOS-based MEMS devices such as pressure sensors, accelerometers, flow sensors and actuators have been widely demonstrated [3, 22–28]. The single crystal silicon-based nanowires could be realized by a top-down approach, i.e. photolithography and etching process technologies from a thin device layer of a silicon-on-insulator (SOI) wafer. Nanoelectromechanical system (NEMS)-based DNA and protein sensors using silicon nanowires (SiNWs) have been reported [29, 30]. Due to the large piezoresistive effect of SiNWs [31–34], using SiNWs as the piezoresistive sensing elements in a pressure-deformable diaphragm was first reported by Soon B *et al* [35]. Soon B *et al* used silicon dioxide (SiO_2) as the diaphragm material as it has a low Young's modulus, which will increase the diaphragm sensitivity. By tuning the carrier concentration of the embedded SiNWs with gate bias applied from the backside of the chip, they demonstrated pressure sensors with extremely high sensitivity. However, the large nonlinear effect shown in the SiNWs would increase the complexity of the read-out circuitry. In addition, the sensor deployed $3.5~\mu m$ buckled-up SiO_2 membrane. The high residual stress introduced by thick thermal SiO_2 layer

made the diaphragm fragile and this has led to very low production yield. Recently a NEMS pressure sensor based on a nanowire field-effect transistor (NWFET) sensing element has been reported with a sensitivity of from 0.019 to 0.079 (mA $A^{-1}~mmHg^{-1}$ when the gate bias of NWFET changes from 0.2 V to −0.2 V [36]. The result shows that the NWFET-based pressure sensor operates at a low bias with higher piezoresistance and can be used to measure low pressures with a high signal noise ratio (SNR). As such, NEMS SiNWs-based pressure sensors provide advantages such as compatible process technology to CMOS manufacturing lines, ultracompact footprint, easy integration of CMOS readout circuitry and high temperature stability. Development of NEMS SiNWs-based pressure sensors can fulfill strong demands from harsh industry applications, e.g. oil well down-hole digger head, to biomedical implants, e.g. sensorized guidewires. In this work, we report the characterization and optimization of a NEMS SiNWs-based piezoresistive pressure sensor of multilayered diaphragm structures using a SiN_x thin film for stress compensation. The pressure sensors have optimized diaphragm with nearly zero-deflection and demonstrate good linearity for the obtained piezoresistive properties of SiNWs.

2. Design, fabrication and measurement set-up

2.1. Microfabrication

The schematic drawing of the pressure sensor is illustrated in figure 1(*a*), while the SEM photo of a microfabricated multilayered diaphragm with a diameter of 200 μm and the optical microscope (OM) photo of a whole device chip are shown in figures 1(*b*) and (*c*) respectively. Figures 1(*d*) and (*e*) show the SEM picture of a 5 μm SiNW after metal deposition and the TEM picture of the SiNW cross section. The multilayered diaphragm comprises the SiN_x layer and the SiO_2 layer. The pressure sensor chip shown in figure 1(*c*) is in square shape with dimensions of 2 mm × 2 mm. The yellow color refers to the SiN_x. The SiNWs are located along ⟨1 1 0⟩ direction at the edge of the diaphragm for maximum strain extraction.

The fabrication process of the diaphragm starts off with a Si (1 0 0) wafer as shown in figure 2. After photolithography, the width of photoresist pattern with respect to the nanowires is about 160 nm. The width of the photoresist pattern is further reduced to 110 nm by using the plasma induced from feeding gas He/O_2 + N_2, where the ratio of He/O_2 is 70/30. The He/O_2 gases are deployed to oxidize the photoresist while the N_2 gas is used to smoothen the surface of the photoresist. This photoresist trimming process allows us to achieve a critical dimension of around 110 nm. After deep reactive ion etching (DRIE) for patterning SiNWs, thermal oxidation is conducted to further shrink down the dimension of SiNWs such that the final cross section of a SiNW is around 90 nm by 90 nm. P-type implantation of dosage 1×10^{14} ion cm^{-2} is then performed using BF_2+, followed by annealing for dopant activation. Next, an extra SiO_2 layer of 4000 Å is deposited for passivation purpose. After via open and metal patterning, a 2.5 μm silicon
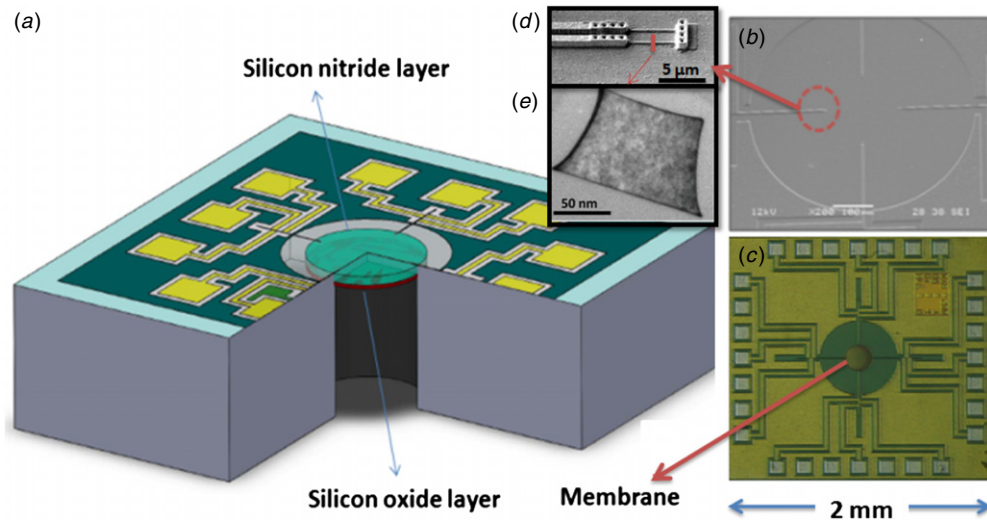
Figure 1. (*a*) Schematic drawing of a pressure sensor, (*b*) a SEM picture of the central part of the pressure sensor, (*c*) an optical picture of the pressure sensor, (*d*) a SEM picture of a 5 m SiNW after metal deposition, and (*e*) a TEM picture of the SiNW.
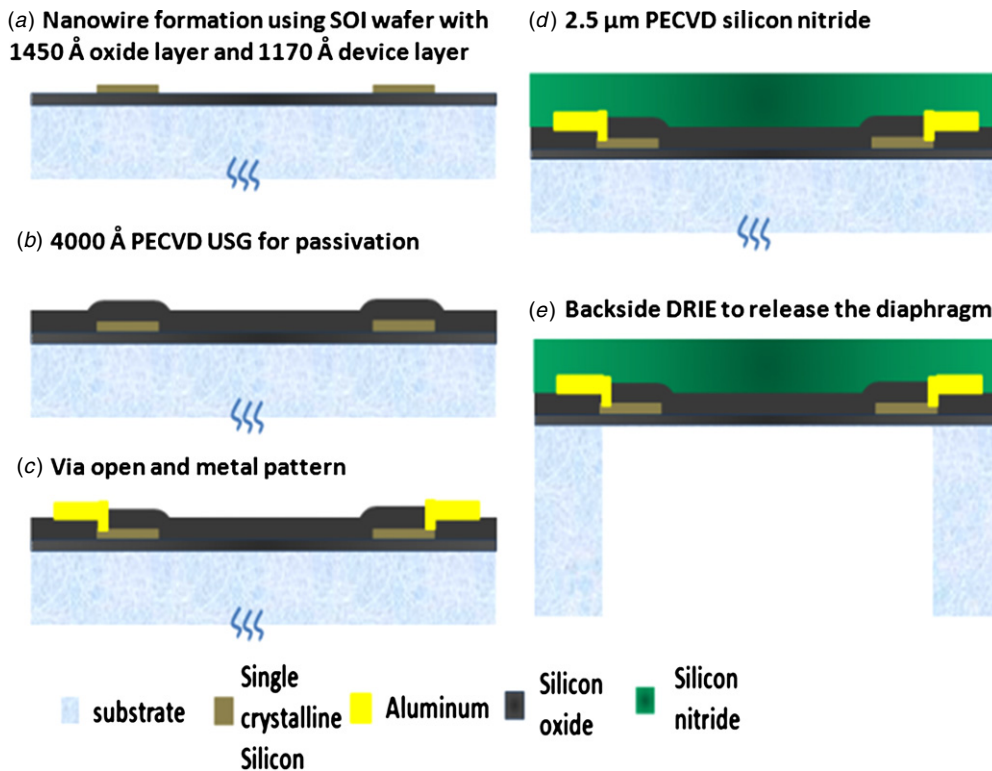
**Figure 2.** Process flow to fabricate the pressure sensor.

nitride film is deposited to compensate the compressive stress in the SiO_2 layer. Finally, DRIE is conducted to release the diaphragm structure. The DRIE process is conducted in a time-controlled manner as the process does not stop effectively on the buried oxide (BOX) layer. The substrate of the wafer is ground to 400 μm before the DRIE process. A total of 350 μm of silicon handle layer is first etched away, with the remaining 50 μm of silicon gradually etched in many etch steps, each of 5 minutes duration. After each etch step, the wafer is taken out and the backside of the wafer is checked under the OM so as to determine whether the entire Si handle layer has been

fully etched away. Figure 3 is obtained by adjusting the focus level to the diaphragm backside through the DRIE hole. Fringe patterns, as seen in figure 3, will be observed under the OM once the entire Si handle layer is fully etched away. These fringe patterns are due to the interference phenomenon of light in the SiO_2 layer.

2.2. Testing set-up

The characterization of the pressure sensor is conducted using the standard bulge testing approach. The testing
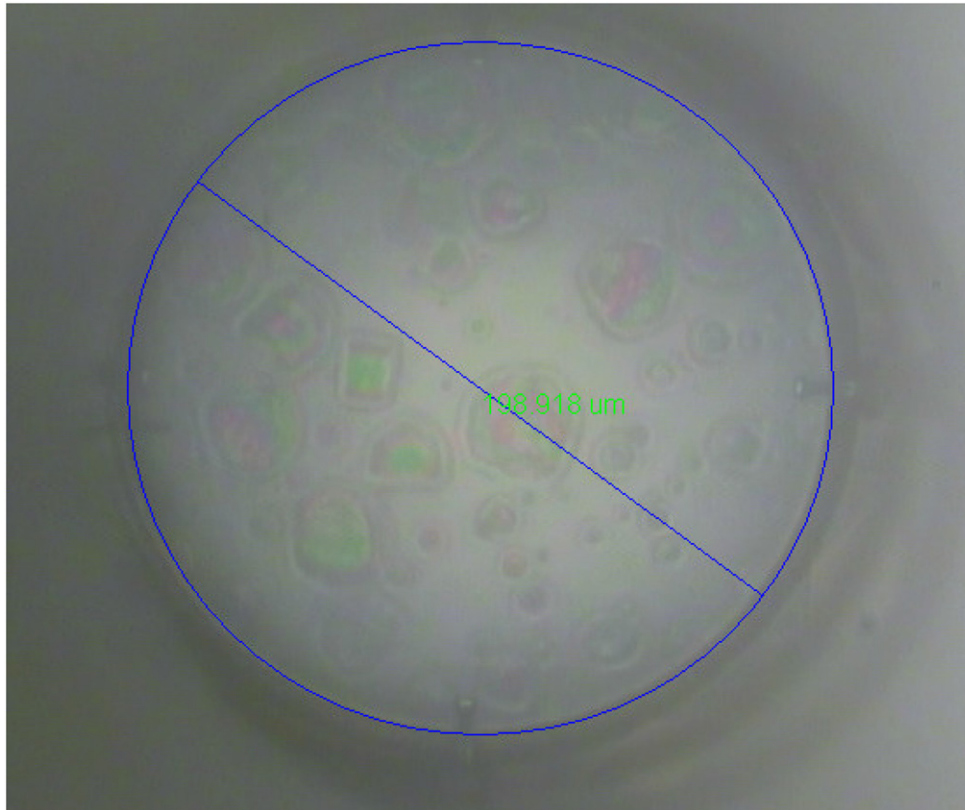
Figure 3. Optical picture of the pressure sensor diaphragm after DRIE upon arrival at the BOX layer.

set-up shown in figure 4(*a*)[4], which consists of a probe station system, a pressure regulator connected to compressed air for pressure application, and the semiconductor parameter analyzer system (Agilent 4156C) for electrical measurement. A specially designed test jig is shown in figure 4(*b*). The jig is assembled using four functional parts: a transparent acrylic plate, an aluminum block with gas inlet, a gasket inside the concave for air sealing and the screws used to fix the plate and the block together. The acrylic plate has an opening window slightly smaller than the chip size. A concave is specially made between the plate and aluminum block for the gasket and the chip. Figure 4(*c*) shows a diced chip, having dimensions of 2.4 cm × 1.0 cm, from one reticle area of the wafer and contains different designs of pressure sensors. It is located and fixed between the gasket and the top acrylic plate is pinned tightly to the aluminum block using the screws. The resistances of the SiNWs are recorded during the experiment while pressure is applied through the gas inlet so as to generate pressure difference against the outer air atmosphere.

---

[4] To apply pressure from the bottom of the testing stage shown in figures 4(*a*) and (*b*) and to deform the top surface of the released diaphragm of the chip toward the cavity encompassed by diaphragm and substrate, the sample with bonded wires has to be assembled upside-down into the testing jig (figure 4(*b*)). The sample preparation procedure is as following: Firstly, the gold wire is bonded onto the metal pad of SiNW, then pulled out to a certain length and cut off, such that we have a fixed end of wire and a free end of wire. Next, the free end the wire is connected to backside of the chip using copper tape; the silver paste is deployed to further fix the wire and for electrical connection at the backside. Finally, the chip is baked in the oven at 90 °C for 15 min to dry the silver paste. After the sample is prepared, it is flipped over and placed inside the test jig.

2.3. FEM modeling

To extract the strain across the diaphragm, especially at the SiNW area, finite element analysis (FEA) using the software ABAQUS is performed. Figure 5(*a*) shows the longitudinal strain of the diaphragm along the ⟨1 1 0⟩ direction under 20 psi uniform pressure, of which the graphical deformation is intentionally enhanced for clearer illustration. The longitudinal component is defined by having the changes of strain and current flow in the same direction. Therefore, this longitudinal strain is distributed along a pair of SiNWs located at exact opposite edge of the diaphragm. Figure 5(*b*) shows the three layer structure model, which comprises 1450 Å BOX layer, 4000 Å oxide layer and different thicknesses of SiN_x layer. Based on this structure, the average strain is extracted and averaged from the corresponding elements at the SiNW area. The Young's modulus and Poisson ratio values used in the modeling are obtained from the literature [47–49] and the residual stress was extracted from warpage of the wafers. FEM modeling is conducted to fit the experiment measurement results and to confirm the accuracy of film parameters used in the FEM modeling.

3. Results and discussion

The design and optimization of geometry for conventional piezoresistors versus the diaphragm dimension have been investigated and reported for bulk and epitaxial silicon [38, 39] as well as for porous silicon [40]. In contrast to
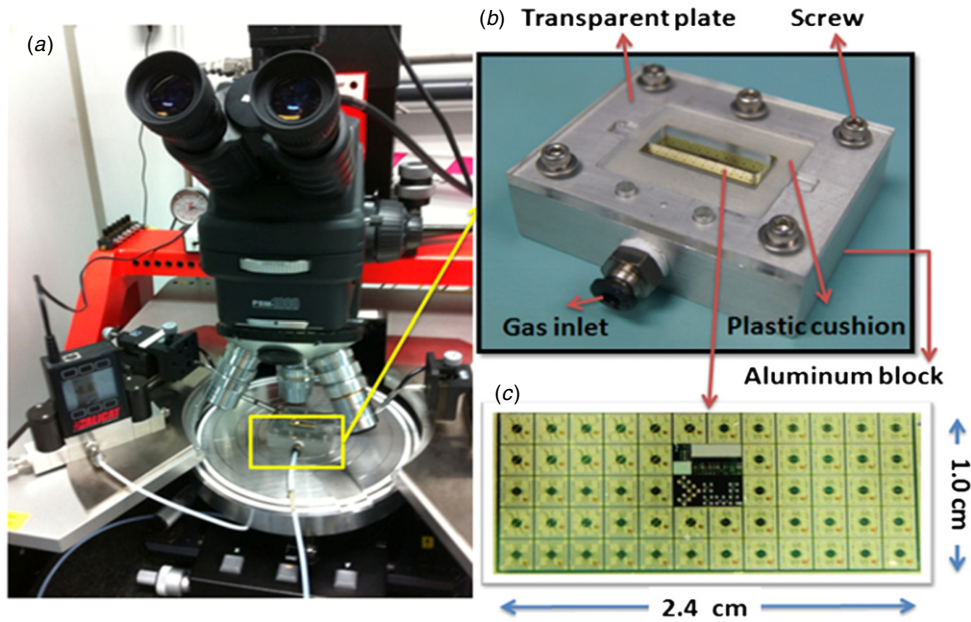
Figure 4. (*a*) The testing set-up on a probe station. (*b*) The test jig for the bulge test. (*c*) A sample of die consisting of the pressure sensors.
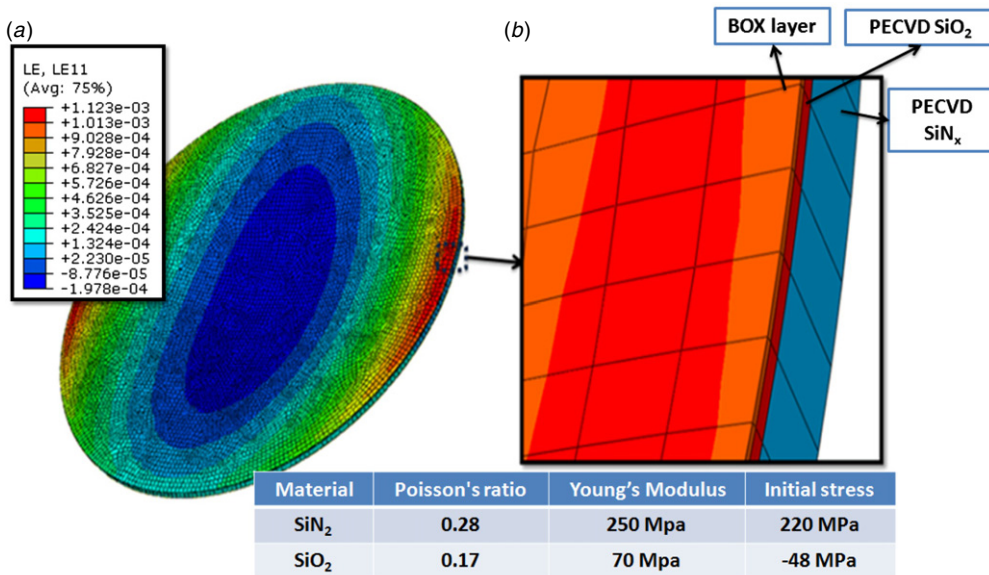

Figure 5. FEM results of (*a*) longitudinal strain distribution of a pressure sensor. (*b*) Zoom-in picture showing the strain distribution at the SiNW area with three-layer meshing. Inset table shows the film parameters.

the optimization of doping concentration for the bulk silicon-based piezoresistors with respect to the geometrical parameters of a silicon flat diaphragm [41] and a SiO_2-on-Si bilayered cantilever structure [42], we are presenting our optimization work for SiNWs-based pressure sensor characterization with respect to doping concentration, length, SiNWs orientation and layer structures of the sensor diaphragm.

3.1. Silicon nanowire optimization

3.1.1. SiNW implantation. Pilot work for nanowire characterization is conducted to optimize the doping level. The BF_2+ is implanted into the silicon with different dosage level ranging from 1×10^{11} ion cm^{-2} to

1×10^{14} ion cm^{-2}. The resistivity of the SiNW is measured as 0.0105 Ω cm, and the doping concentration of the SiNW is calculated as 7.87×10^{18} ion cm^{-3} accordingly [43]. *I–V* curves of 5 μm SiNWs (shown in figure 6) at the wafer edge and center are measured accordingly using the parameter analyzer. Small voltage sweep from -1.5 V to $+1.5$ V is applied to the SiNWs to avoid a joule heating effect. As observed, the SiNWs at 1×10^{14} ion cm^{-2} dosage shows very good linearity, indicating its performance as a pure resistor. In addition, the *I–V* curves extracted from the wafer center and edge perfectly overlapped each other, indicating good uniformity across the wafer. In contrast, when the SiNW dosage level is only at 1×10^{11} ion cm^{-2}, or even without any doping, i.e. at an intrinsic state, the SiNW shows
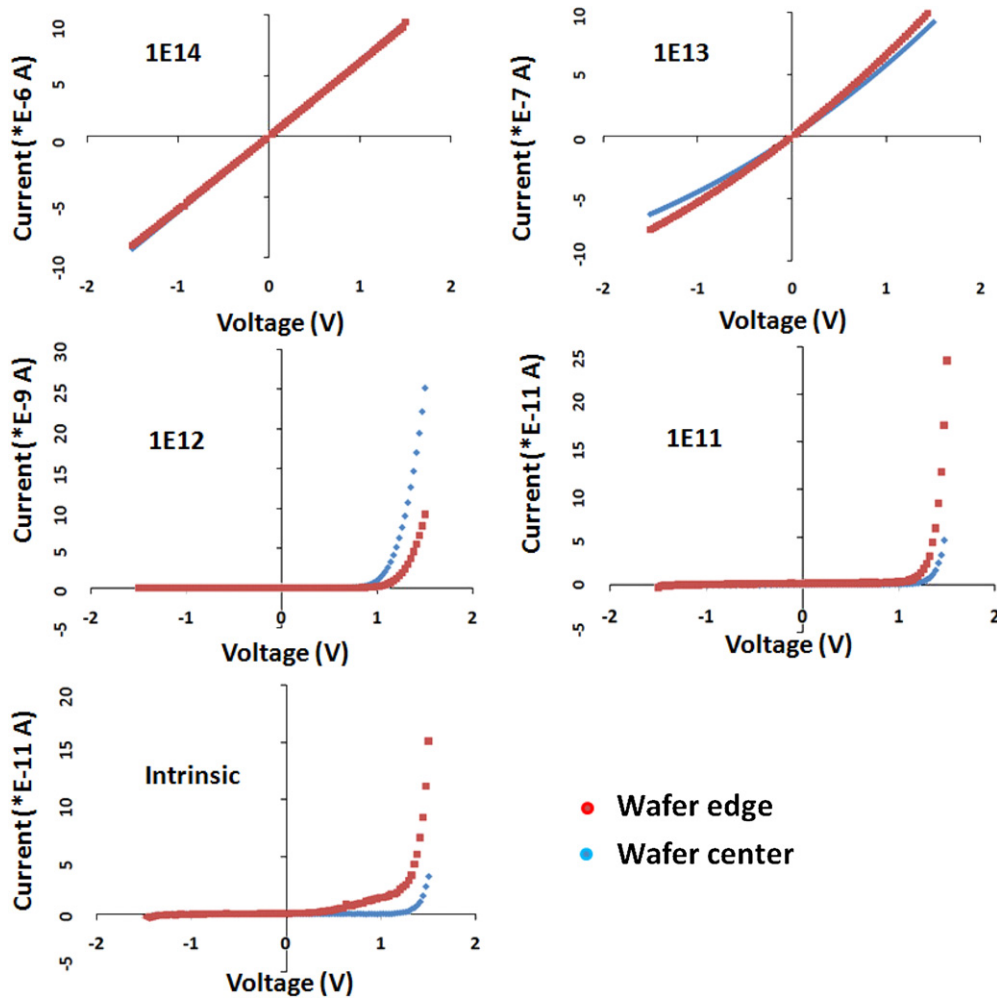
Figure 6. I–V curve measurement of SiNW with different dosage of implantation from (*a*) 1×10^{14} ion cm^{-2}, (*b*) 1×10^{13} ion cm^{-2}, (*c*) 1×10^{12} ion cm^{-2}, (*d*) 1×10^{11} ion cm^{-2}, (*e*) intrinsic.

rather high resistance, resulting in a very low current of picoampere magnitude with obvious nonlinear biasing range. The center to edge variation also becomes more distinct when the dosage drops. The *I–V* curves of SiNW with clear nonlinear phenomena are probably due to the Schottky effect. This is especially obvious for the intrinsic SiNW and SiNWs with doping of 1×10^{11} ion cm^{-2} and 1×10^{12} ion cm^{-2}, i.e. figures 6(*c*)–(*e*). As the positive bias increases, the width of the Schottky barrier becomes narrower. This is evident from the tunneling effect appearing at around 1.5 V where the sudden current jump shows. In contrast, the negative bias makes the tunneling current relatively harder to form because it tends to widen the width of the barrier. Thus the current jump does not show in the negative voltage region in the *I–V* curve.

Neuzil *et al* [34] reported a giant gauge factor piezoresistive effect of SiNWs up to 5000 by shrinking cross-sectional dimensions, low dosage condition at 1×10^{12} ion cm^{-2} and applying back-gate bias voltage. However, such SiNWs with giant gauge factor are also very sensitive to noise because of a low dosage. After considering the complexity and stringent measurement conditions required by the high gauge factor with back-gate bias, we present our SiNWs-based pressure sensor with no bias applied. This simplifies

the connections and makes the sensor signal output more immune to noise. Such biased condition could be designed for future applications that require a higher gauge factor in a more controlled environment.

3.1.2. SiNW length. With the advantage of good scalability, the SiNWs can be accurately placed at a specific position in the membrane for a target strain extraction. In this test, the SiNWs are located between bottom 1450 Å BOX layer and 4000 Å PECVD passivation oxide layer with another 2.5 μm SiN$_x$ on top. This thin BOX layer facilitates that the SiNWs are located away from the diaphragm neutral axis. Additionally, this enables the feasibility of further reduction of diaphragm thickness at a given diameter without compromising the device performance. As mentioned above, the SiNWs with the cross section of 90 nm by 90 nm are located at the diaphragm edge to maximize the applied strain. To explore the sensitivity dependence upon SiNWs length, 0–20 psi pressure is applied to the sensors with SiNWs length of 1 μm, 2 μm, 5 μm and 10 μm along the $\langle 1\,1\,0 \rangle$ direction. Figure 7 shows the results of pressure sensor characterized under a standard bulge test. As observed from figure 7, 1 μm SiNWs-based design has the
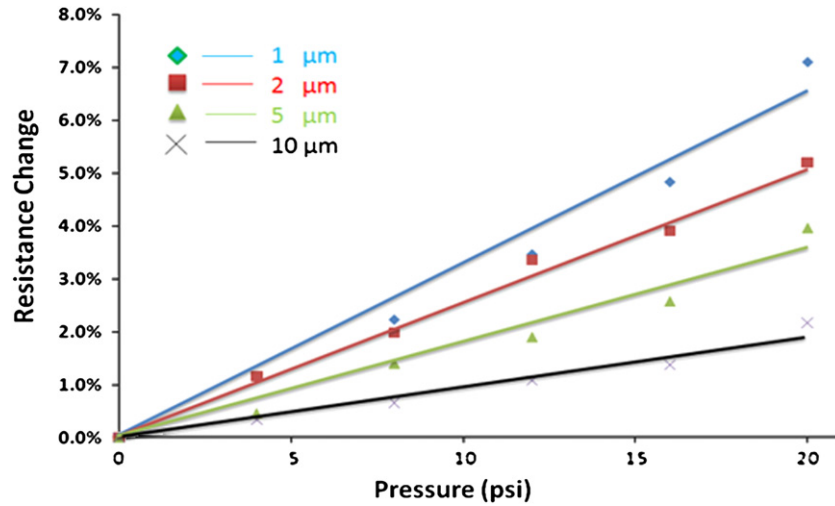
Figure 7. The resistance change against applied pressure with SiNW lengths of 1 μm, 2 μm, 5 μm and 10 μm respectively.
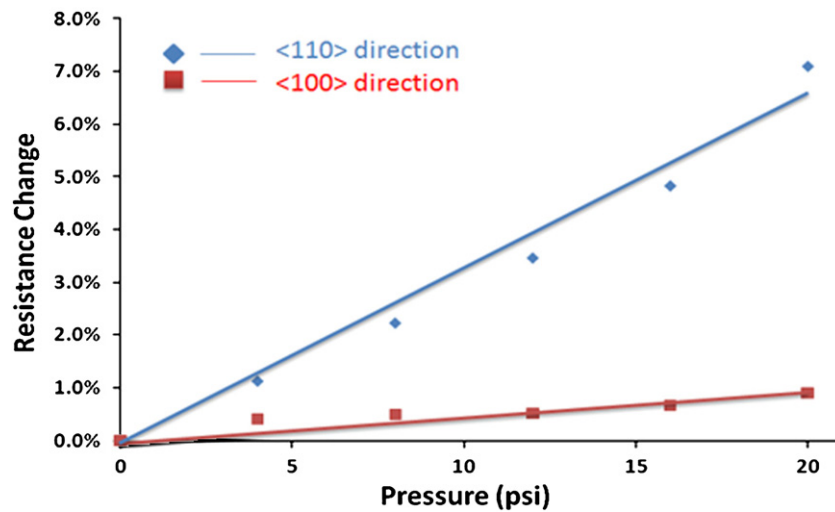

Figure 8. The resistance change against pressure for sensors with SiNWs along the $\langle 1\,1\,0 \rangle$ and $\langle 1\,0\,0 \rangle$ directions.

highest sensitivity while the 10 μm one has the lowest one. Here the sensitivity of the pressure sensor is defined as

$$S = \frac{\Delta R/R}{\Delta P}. \tag{1}$$

where S represents the sensitivity, R refers to the SiNW resistance and P is the differential pressure uniformly applied to the diaphragm.

Using such definition, the sensitivities for 1 μm, 2 μm, 5 μm and 10 μm SiNW pressure sensors are 0.32% psi^{-1}, 0.25% psi^{-1}, 0.15% psi^{-1}, and 0.09% psi^{-1}, respectively. This is due to the decreasing distribution of the stress from the diaphragm edge to center. Hence, the shortest SiNWs with a length of 1 μm experience the largest average stress. The same explanation also applies in strain distribution. As a result, a gauge factor as large as 78 is extracted from 1 μm SiNWs, whereas in cases of SiNW with other lengths, the integration should be considered for more precise calculation. We also did four-point bending testing which gives a similar gauge factor for SiNW with different lengths by utilizing the uniform stress application from such a set-up [41].

3.1.3. SiNW orientation. Single crystal silicon has a high gauge factor, which makes it well suited to enable high-sensitivity piezoresistive devices. However, the orientation dependence of single-crystal silicon must also be taken into account. Many research studies have been performed regarding the effect of different orientations on SiNWs performance. Kanda plotted the piezoresistive coefficient in arbitrary directions on the commonly used (1 0 0) crystal plane graph [44]. Our results match their study in comparison on piezoresistive between $\langle 1\,1\,0 \rangle$ and $\langle 1\,0\,0 \rangle$ SiNWs direction. Figure 8 shows that the bulge testing results of pressure sensors with 1 μm SiNWs along both orientations. Based on our measurement, the sensitivity of 1 μm SiNWs in $\langle 1\,1\,0 \rangle$ direction is 0.32% psi^{-1}, whereas the sensitivity of same length SiNWs in $\langle 1\,0\,0 \rangle$ only has 0.046% psi^{-1}. This difference is as huge as seven times.

3.1.4. Temperature effect of the SiNW. To avoid the joule heating effect during measurement, the sweep of voltage should be controlled within a small range, and the sampling points and sampling time should be minimized. Besides, if
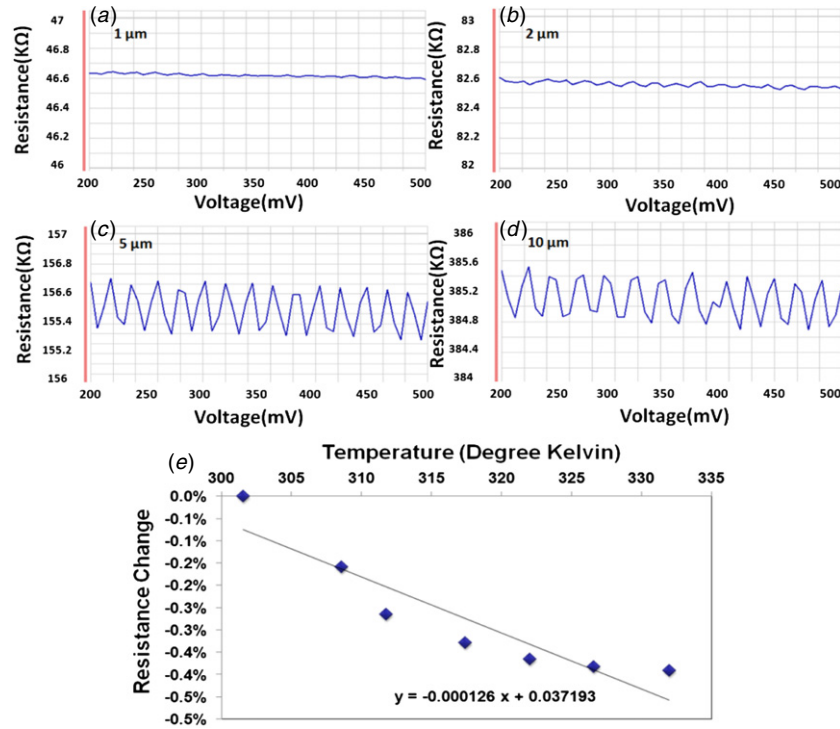
Figure 9. (*a*)–(*d*) The resistances of SiNWs with lengths of 1 μm, 2 μm, 5 μm and 10 μm against bias voltage from 0.2 V to 0.5 V (*e*) The resistance change of the 2 μm SiNW against temperature.

the measurement voltage is too low, the SiNW is relatively vulnerable to surrounding noise. Thus in our measurement, we adopt a bias voltage from 0.2 V to 0.5 V. During the testing, 51 points are taken with sampling time of 10 μs for each data point. The resistances of SiNWs with length of 1 μm, 2 μm, 5 μm and 10 μm against applied voltage are shown in figures 9(*a*)–(*d*) respectively. As can be seen, the resistance change during the sweep is quite small, i.e. within 0.1%. Such resistance change is negligible in comparison of the measurement range of the pressure sensor. To further study the heating effect of the SiNW during measurement, the data of 2 μm SiNW are used to obtain the temperature coefficient of resistance (TCR). The experiment is conducted in a vacuum chamber with a heater and a temperature sensor. The sample is stabilized for half an hour for each target temperature step from 300 K to 330 K. Labview software is adopted to record the resistance change against the temperature. The measured data are shown in figure 9(*e*). Although a clear nonlinear relationship is observed as the temperature increases, the TCR extracted is around −0.0126% K^{-1} by linear fitting. Furthermore, the SiNW is surrounded in the oxide, which helps to release the generated heat compared to the suspended SiNW exposed to air. This helps explain the relatively small temperature effect in our measurement.

3.2. Diaphragm optimization

3.2.1. Single SiO$_2$ layer versus multilayered diaphragm. As introduced in the fabrication process flow, a dielectric layer is deposited for the purpose of diaphragm formation and metal passivation. The commonly used dielectric materials include SiO$_2$ and SiN$_x$. Due to internal stress difference,

i.e. compressive stress for SiO$_2$ and tensile stress for SiN$_x$. Different thicknesses of each material are tried in our fabrication. A white light interferometer (VEECO NT3300) system is used to record the surface profile. Figure 10 illustrates the comparison of the diaphragms made of a pure oxide layer and SiN$_x$-SiO$_2$ combined layer. The pure SiO$_2$ fabricated diaphragm has the merit of higher sensitivity due to its relatively low Young's modulus. However, such diaphragm suffers from buckling and wrinkling issues due to its internal compressive stress. Ziebart V *et al* discussed the buckling state of diaphragm in detail and classified the buckling states based on the symmetry property of the diaphragm, i.e. reflection symmetry and rotation symmetry [45]. Accordingly, we define the diaphragm without reflection and rotation symmetry as a wrinkled state. Figure 10(*a*) shows the 3D picture of a 3 μm SiO$_2$ diaphragm with obvious buckling profile. Such buckling in both upward and downward directions are observed as shown in top views of figures 10(*b*) and (*c*) respectively. The red color represents a higher deflection for out of surface direction while the blue color refers to a lower deflection in the same direction. To compensate the internal compressive stress of SiO$_2$, a 2.5 μm SiN$_x$ layer with 220 MPa internal tensile stress is deposited on top of the 0.5 μm SiO$_2$ layer. The 3D picture of the bilayered diaphragm with nearly zero deflection is fabricated as shown in figure 10(*d*). The uniform blue color implies the flat topography of the diaphragm. The central deflection of such diaphragm is smaller than 0.05 μm.

Table 1 shows our optimization work on diaphragms made of different combinations of the BOX layer and SiO$_2$/SiN$_x$ layer. The diaphragm using 1.4 μm SiO$_2$ (1 μm BOX plus 0.4 μm PECVD oxide passivation layer) before further deposition shows the largest deformation with the highest
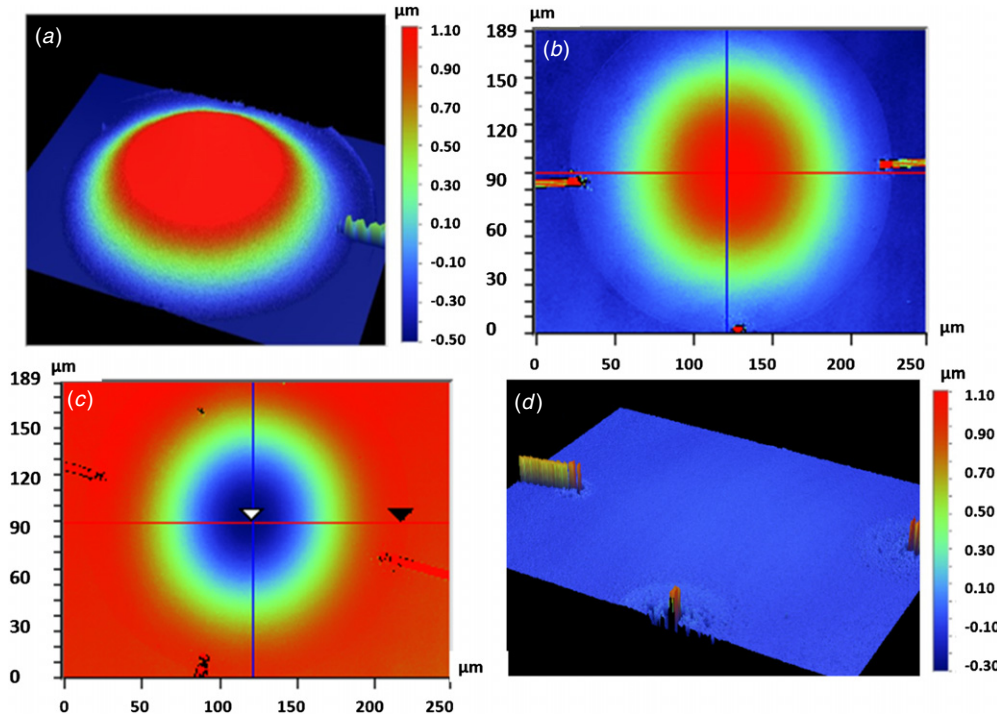
Figure 10. (*a*) The 3D picture of buckled diaphragm made of pure oxide (*b*) and (*c*). The top view of the buckled (*b*) up and (*c*) down diaphragm (*d*) The 3D picture of the diaphragm with a 2.5 μm SiN$_x$ layer.

**Table 1.** The diaphragm results of different combination of BOX and deposition layer.

Thickness of oxide layer	Type and thickness of deposition layer	Deflection profile
1.4 μm	Without oxide or nitride	Asymmetric membrane at a wrinkled state with 6.1 μm deflection at maximum
1.4 μm	1.5 μm PECVD oxide	Nonconcentric buckled diaphragm with 2.5 μm deflection at maximum
1.4 μm	2.5 μm PECVD oxide	Concentric buckled diaphragm with 1.7 μm central deflection
1.4 μm	2.5 μm PECVD nitride	Cocentric buckled diaphragm with 0.1 μm central deflection
5450 Å	2.5 μm PECVD nitride	Concentric buckled diaphragm with central deflection smaller than 0.1 μm

deflection point of 6.1 μm and the asymmetric diaphragm shape refers to a wrinkled state. The oxide deposition on top helps reduce the wrinkling situation. However, the diaphragms still show deflections of 1.7 μm for 2.5 μm thick oxide layer and 2.5 μm for 1.5 μm thick oxide layer. This situation is drastically improved with the help of internal tensile stress of PECVD nitride. As can be seen from table 1, 2.5 μm SiN$_x$ with 1 μm BOX and 1450 Å BOX give only 0.1 μm and 0.05 μm deflection respectively, which are 1 order of magnitude smaller than the diaphragm with oxide deposition.

3.2.2. Effect of SiN$_x$ layer thickness. To investigate the surface profile of the SiN$_x$ layer with different thickness on oxide layer, one die with original SiN$_x$ thickness of 2.5 μm is chosen and etched using CHF$_3$ reactive ion etch (RIE) to thin down the nitride thickness based on time control. Firstly, 30 min of RIE etch is conducted and the results are shown in the optical and 3D profile pictures in figures 11(*a*) and (*d*). After 15 min, the SiN$_x$ layer is fully removed and the corresponding results are shown in figures 11(*b*) and (*e*). Finally, an extra 15 min is added in order to see the surface profile of the further thinned down diaphragm. In figure 11(*f*),

the surface profiler picture cannot be fully recorded because of the large deflection exceeding the equipment limitation, but the wrinkling status can be clearly observed. These three pairs of diaphragm pictures show clear transformation from a regular diaphragm of good flatness into a wrinkled diaphragm of irregular deformation, with respect to RIE etching time increment. It is worth noting that, in figures 11(*b*) and (*e*), the edge of diaphragm is in a star shape after the SiN$_x$ is just stripped, indicating the stress distribution inside the SiO$_2$ layer along the membrane edge. The star-shape shows the onset stage in between the flat multilayered diaphragm and the wrinkled diaphragm. After the SiN$_x$ layer is stripped, the membranes swelling in both upward and downward directions are observed as well.

To quantitatively explore the relationship between the diaphragm deflection and the SiN$_x$ thickness, the top view of profiles and vertical deflection of the multilayered diaphragms with SiN$_x$ layers of various thicknesses are recorded and shown in the inset of figure 12. The sample is placed with some rotation to avoid the height jump at the SiNWs and the junction of electrical connection location. The vertical deflection at the diaphragm center increases from 0.05 μm to 4.90 μm with respect to the SiN$_x$ layer thickness decreasing
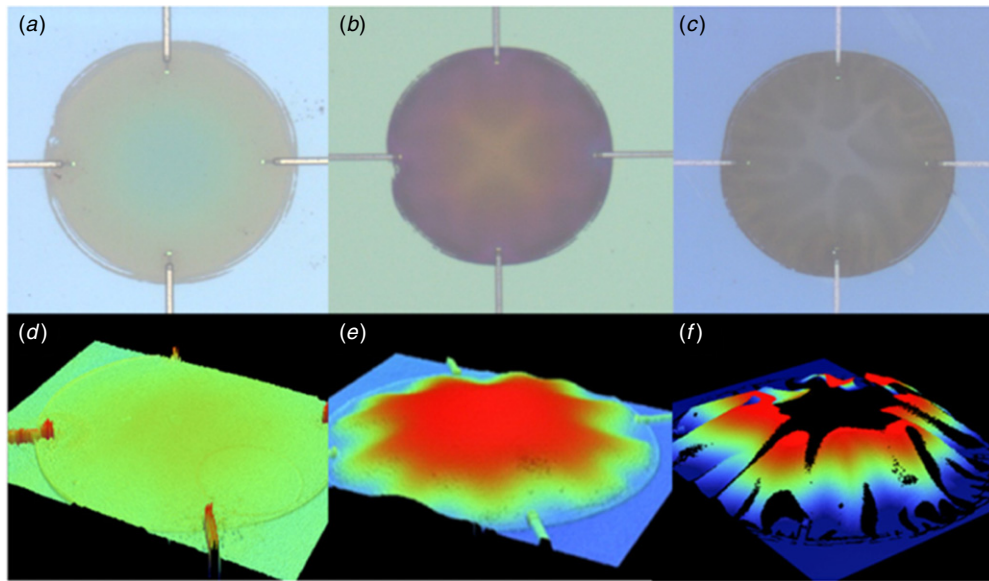
Figure 11. (*a*) and (*d*), (*b*) and (*e*), (*c*) and (*f*) show the optical picture and 3D profiler picture of the diaphragms after 30 min, 45 min and 60 min SiN$_x$ layer etch respectively.
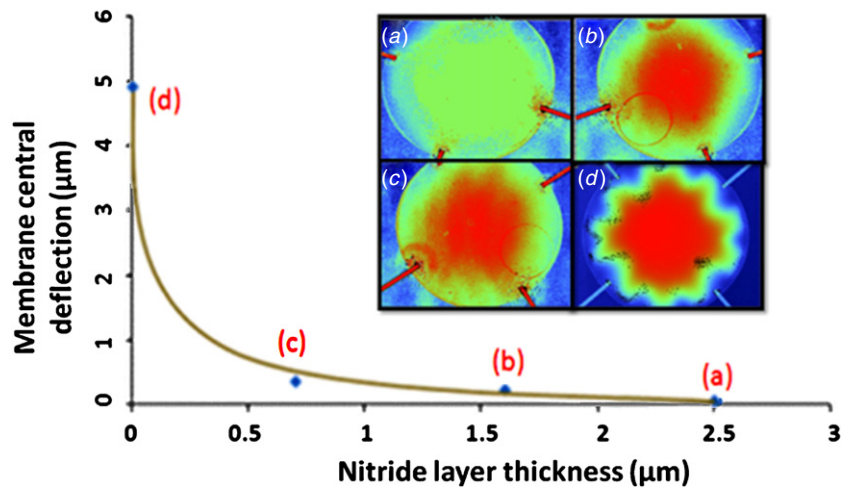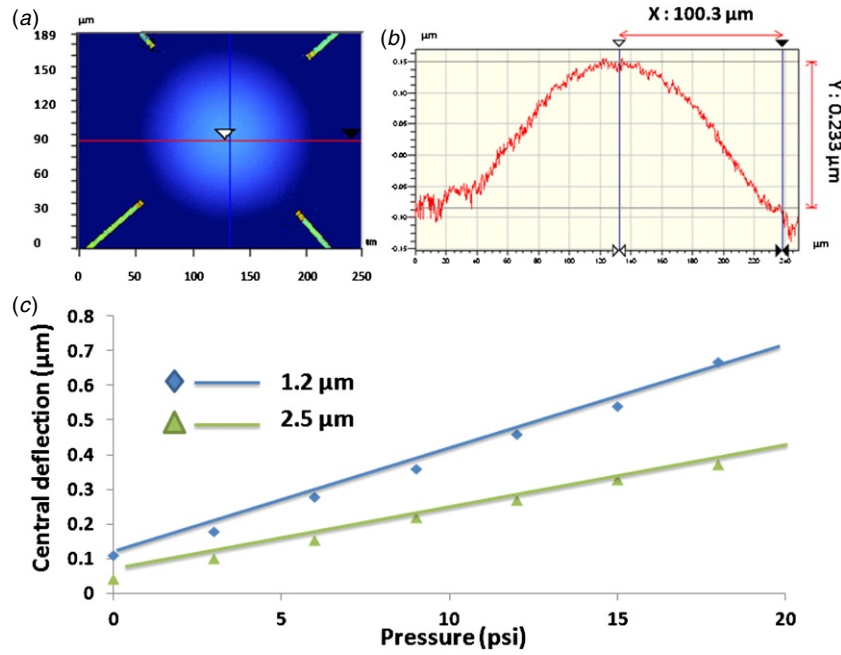

Figure 12. Diaphragm central deflection against SiN$_x$ layers with various thicknesses.

from 2.5 μm to 0 μm. By fitting the scattered data, we can clearly observe that the membrane central deflection change is relatively small within the range, where the thickness of the SiN$_x$ layer varies from 2.5 μm to 0.7 μm. However, the deflection jumps from around 0.4 μm to nearly 5 μm as the thickness of the SiN$_x$ film is further thinned down from 0.7 μm to 0 μm. After the diaphragm is further etched into the wrinkled state, maximum deflection point as high as 8.3 μm is observed. This clear nonlinear relationship indicates that the SiN$_x$ layer is able to modulate the diaphragm profile in an effective manner before thickness of SiN$_x$ reaches 0.5 μm; whereas in the case of deposition of more than 0.5 μm SiN$_x$, the improvement becomes less effective. In addition, in comparison with the concentric profile of 1.6 μm SiN$_x$ diaphragm, a nonconcentric profile is shown with 0.7 μm SiN$_x$ as in the inset of figure 12(*c*). Such a nonconcentric profile will make the diaphragm potentially impractical for real situation in the long run. Although the

thicker SiN$_x$ layer will lower the pressure sensor sensitivity due to the bending stiffness increase, decreasing the thickness of SiN$_x$ by a large amount will reduce the linear region and overall working range. These considerations indicate compromises should be made to choose an appropriate thickness of the SiN$_x$ layer and it will be discussed in the following parts. The etching-back approach using one die helps avoid the chip variation across the wafer during the fabrication process. Most importantly, it saves the effort and resources to fabricate a batch of whole pieces of devices by depositing the SiN$_x$ layer with different thickness. Following this guideline, we verified the results in one later version of short-loop fabrication of a 1 μm SiN$_x$ diaphragm without SiNW. The diaphragm shows very similar results, i.e. around 0.1 μm central deflection for 1 μm SiN$_x$ layer deposition. Furthermore, in order to find the working range of pressure sensor with 2.5 μm SiN$_x$, the fracture test will be conducted. In the test, the tungsten needle with tip diameter of 300 nm is manipulated by PI E-517

Figure 13. (*a*) The top view of the diaphragm under 12 psi pressure application. (*b*) The profile along the red line in (*a*). (*c*) The central deflection against the applied pressure for diaphragms with 1.2 μm and 2.5 μm SiN$_x$ layer respectively.

Digital Piezo Controller to push the diaphragm in top down direction. The diaphragm fracture point with respect to needle tip displacement will be explored in discussion of the pressure sensor working range section.

3.2.3. Surface profile versus applied pressure. To explore the diaphragm profile change against the applied pressure with different thickness, the diaphragms with SiN$_x$ layer of 1.2 μm and 2.5 μm in thickness are studied respectively. The measurement results are shown in figure 13. Based on the plate theory, the diaphragm displacement in the perpendicular direction is considered to be in a linear relationship against the applied pressure when its central deflection is smaller than the diaphragm thickness [46]. The governing formula is given in equation (2) as follows:

$$w(r) = \frac{Pa^4}{64D} \left[1 - \left(\frac{r}{a} \right)^2 \right]^2. \quad (2)$$

where w is the displacement, r and a denote the radial coordinate and diaphragm radius respectively, P is the uniform differential pressure applied to the diaphragm, D is the flexural rigidity, which is a stiffness measurement and is expressed in the equation

$$D = \frac{Eh^3}{12(1 - v^2)} \quad (3)$$

where E is the Young's modulus, v is the Poisson's Ratio and h is the total thickness of the diaphragm. Since we have diaphragm consisting of double layers, the bending stiffness should be adjusted accordingly as in the equation (4) [47]

$$D = \frac{E_{ps,1}^2 h_1^4 + E_{ps,2}^2 h_2^4}{12(E_{ps,1} h_1 + E_{ps,2} h_2)}$$
$$+ \frac{E_{ps,1} E_{ps,2} h_1 h_2 \left(2h_1^2 + 3h_1 h_2 + 2h_2^2 \right)}{6 \left(E_{ps,1} h_1 + E_{ps,2} h_2 \right)}. \quad (4)$$

where h_1 and h_2 are the thicknesses of the SiO$_2$ and SiN$_x$ layers respectively. E_1, E_2 and v_1, v_2 denote the Young's modulus and Poisson's Ratio accordingly. The plane-strain moduli are $E_{ps,1} = E_1 / (1 - v_1^2)$. and $E_{ps,2} = E_2 / (1 - v_2^2)$. Given that SiN$_x$ has Young's modulus of 250 GPa and SiO$_2$ 70 GPa, Possion's ratio as 0.28 and 0.17 [47, 48], the central deflection of diaphragms with 2.5 μm SiN$_x$ and 1.2 um SiN$_x$ are calculated as 0.42 μm and 0.99 μm, which are in good agreement with measurement data under 20 psi pressure. Figures 13(*a*) and (*b*) show a typical profile across the diaphragm when the pressure application is 12 psi with SiN$_x$ thickness of 2.5 μm. As seen in figure 13(*c*), the measured data in both cases give smaller deflection than their respective thicknesses, which indicates a reasonable linear relationship within the measurement range.

3.2.4. Sensitivity versus SiN$_x$ layer thickness. As mentioned above, the sensitivity of the pressure sensor is closely related to the diaphragm thickness. To explore experimentally such a relationship, the pressure sensors with 1 μm SiNW and two kinds of SiN$_x$ layer thickness, i.e. 2.5 μm and 1.2 μm, are investigated. The sensitivity derived from the linear fitting lines shows increment from 0.3% psi^{-1} to 0.6% psi^{-1} as the SiN$_x$ layer thickness reduced from 2.5 μm to 1.2 μm (shown in figure 14). Such data are in good agreement with the simulation results. It is also observed that the sensitivity doubles as the thickness of SiN$_x$ reduces by almost a half. This could imply the proportionality between variations of SiN$_x$ layer thicknesses against the sensitivity changes. In comparison with the data of 0.1 mV/V/psi^{-1} in [14], we achieve a sensitivity of 1.5 mV/V/psi^{-1}, which is 15 times better. Moreover, as we mentioned in previous section, this improved sensitivity does not compensate much trade-off in diaphragm deflection. Therefore, it is a good compromise in terms of sensing range, sensor sensitivity and surface profile optimization.
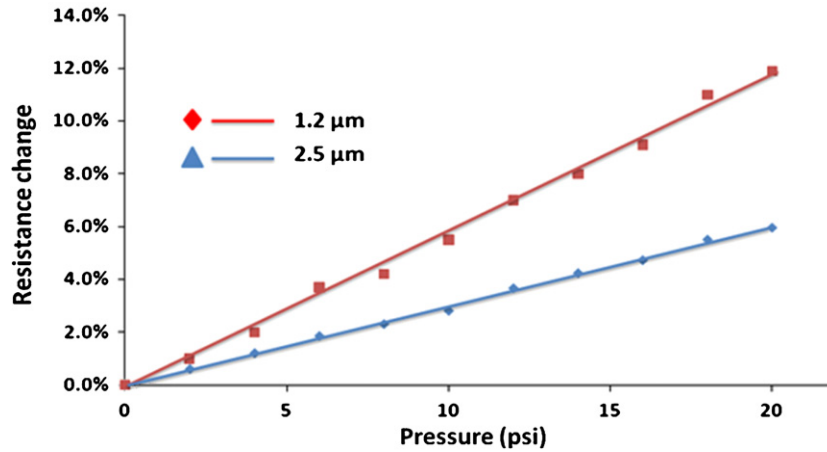
Figure 14. The pressure sensor bulge testing results of 1.2 μm SiN$_x$ layer and 2.5 μm SiN$_x$ layer.
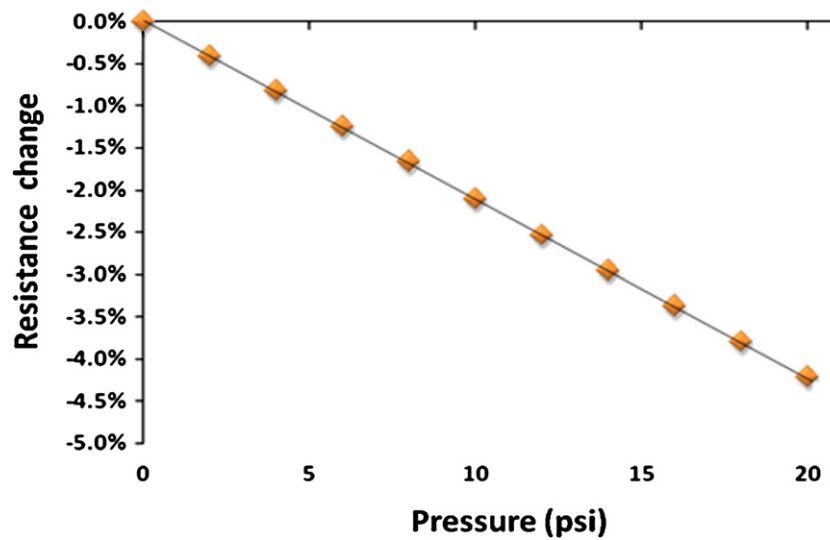

Figure 15. The pressure sensor characterized in the compressive strain region by using the reverse direction the bulge test.

3.3. Reverse direction characterization and working range in the compressive strain region

3.3.1. Reverse direction bulge test. For most pressure sensor characterization, the pressure is applied along single direction due to the set-up limitation. Consequently, the pressure sensor behavior in both directions is not fully revealed. In this work, the tested sample is flipped over with electrical signal connected out from bonding wire. Hence, we are able to overcome the set-up limitation and apply the pressure test in both front side and back side directions [49]. As shown in figure 15, the reverse direction testing results also show very good linearity within our measurement range in comparison with the normal bulge testing results. Besides, this approach applies more closely to real situation, e.g. the eye pressure measurement using such pressure sensor, where the pressure is applied perpendicular to diaphragm along the front side direction.

3.3.2. Working range of pressure sensor under compressive strain. By confining the SiNWs between 1450 Å box and 4000 Å oxide layer with 2.5 μm SiN$_x$ on top, this flat

diaphragm structure could sustain a large compressive/tensile strain to the extent before the diaphragm reaches the fracture point without buckling issues [47, 48, 51]. When the diaphragm is deformed due to the force transferred from needle tip, strain is transmitted to the SiNWs. Thus the SiNWs resistance change can be detected and is used as an indicator to define the moment when needle tip makes physical contact on the diaphragm. The experiment is also conducted on the probe station platform under the optical microscope. The tip is carefully aligned to be positioned directly on top of the center of the membrane and moves in perpendicular to the membrane with 1 μm displacement in each step. Figure 16 shows the measured resistance change against tip displacement for the two sensor chips with 2 μm and 5 μm SiNWs respectively. The resistance of SiNWs remains constant until the on-set point at about 2.0 μm tip displacement. This indicates that the force introduced by the needle tip has led to measurable strain changes onto the SiNWs. As greater displacement is applied to needle tip continuously, the resistance keeps dropping down to 17.7% for the sample of 5 μm SiNWs and to 15.8% for the sample of 2 μm SiNWs respectively. Eventually the diaphragm breaks when the tip displacement reaches at 22 μm and
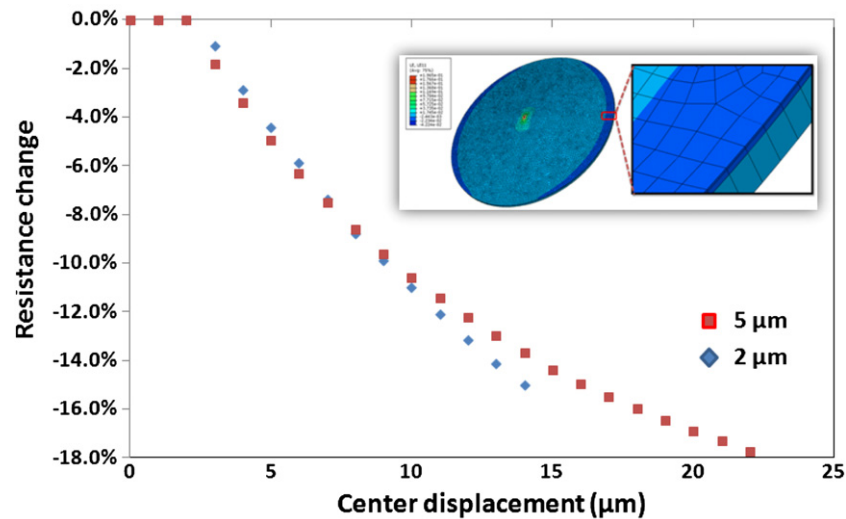
Figure 16. The SiNW resistance change when using PZT driven tip to apply displacement at the diaphragm center.

14 μm, i.e. a diaphragm center displacement of 20 μm and 12 μm accordingly.

The formula for obtaining the burst pressure to the pressure sensor is given by the following equation [50]:

$$BP = \frac{3.4}{1 - v^2} \frac{\sigma_{\text{MAX}} t^2}{A} \qquad (5)$$

where *BP* is the burst pressure, *t* is the thickness of the diaphragm, *A* is the area of the diaphragm, σ_{MAX} is the maximum nondestructive Von mises stress to the SiN_x film. The value, σ_{MAX} was extracted from a combination of the central displacement testing and the FEM modeling of the SiN_x layer. In the experiment, the diaphragm is usually fractured at the diaphragm edge, with central displacement higher than 12 μm. With the central displacement of 12 μm, the Von mises stress was extracted from the elements of the SiN_x layer at the diaphragm edge from the FEM modeling. The value was averaged to be around 3100 MPa. Substituting the SiN_x layer thickness of 2.5 μm, a diaphragm diameter of 200 μm and Poisson ratio 0.28 into equation (5), the burst pressure is calculated as 330 psi. Because the diaphragm comprises the 2.5 μm SiN_x layer and 5450 Å SiO_2 layer, the actual stiffness of the diaphragm is even larger. It implies that the burst pressure of the pressure sensor should be above 330 psi, indicating a very high mechanical strength of the diaphragm that is able to survive a very high pressure without damage.

4. Conclusion

In this paper, we characterized a pressure senor using SiNWs as the sensing element. After exploring and discussion on the effects of doping concentration, length difference and orientation variations, $\langle 1\,1\,0 \rangle$ direction SiNWs with length of 1 μm and dosage of 1×10^{14} ions cm^{-2} have been determined as optimized sensing elements. In order to maximize the sensitivity and also retain minimized (or acceptable) diaphragm deflection as well as reasonable device working range, a trade-off for the thickness of multilayered diaphragm has been studied step by step. As a result, the

diaphragm with compromised SiN_x thickness of 1.2 μm shows not only an almost flat surface profile, but also a high sensitivity as good as 0.6% psi^{-1}, which is 15 times larger than that in the reported data. In addition, the front side pressure measurement approach is also introduced. This enables our device to be tested in dual directions. Such results are more meaningful in real-life practical applications. Finally, further fracture test proves that our device is able to sustain the pressure above 330 psi.

References

[1] Smith C S 1954 Piezoresistance effect in germanium and silicon *Phys. Rev.* **94** 42–9
[2] Peake E R, Zias A R and Egan J V 1969 Solid-state digital pressure transducer *IEEE Trans. Electron Devices* **16** 870–6
[3] Barlian A A, Park W-T, Mallon J R, Rastegar A J Jr and Pruitt B L 2009 Review: semiconductor piezoresistance for microsystems *Proc. IEEE* **97** 513–52
[4] Fleming W J 2001 Overview of automotive sensors *IEEE Sensors J.* **1** 296–308
[5] Esashi M, Sugiyama S, Ikeda K, Wang Y and Miyashita H 1998 Vacuum-sealed silicon micromachined pressure sensors *Proc. IEEE* **86** 1627–39
[6] Eddy D and Sparks D 1998 Applications of MEMS technology in automotive sensors and actuators *Proc. IEEE* **86** 1747–55
[7] Eaton W P and Smith J H 1997 Micromachined pressure sensors: review and recent developments *Smart Mater. Struct.* **6** 530–9
[8] Marco S, Samitier J, Ruiz O, Morante J R and Steve J E 1996 High performance piezoresistive pressure sensors for

biomedical applications using very thin structured membranes *Meas. Sci. Technol.* **7** 1195–203

[9] Katuri K C, Asrani S and Ramasubramanian M K 2008 Intraocular pressure monitoring sensors *IEEE Sensors J.* **8** 12–9

[10] Peng C, Ko W H and Young D J 2010 Wireless batteryless implantable blood pressure monitoring microsystem for small laboratory animals *IEEE Sensors J* **10** 243–54

[11] Chatzandroulis S, Tsoukalas D and Neukomm P A 2000 A miniature pressure system with a capacitive sensor and a passive telemetry link for use in implantable applications *IEEE J. Microelectromech. Syst.* **9** 18–23

[12] Samaun , Wise K D and Angell J B 1973 IC piezoresistive pressure sensor for biomedical instrumentation *IEEE Trans. Biomed. Eng.* **BME-20** 101–9

[13] Borky J and Wise K D 1979 Integrated signal conditioning for silicon pressure sensors *IEEE Trans. Electron Devices* **ED-26** 1906–10

[14] Kalvesten E, Smith L, Tenerz L and Stemme G 1998 The first surface micromachined pressure sensor for cardiovascular pressure measurements *Proc. of IEEE MEMS 98 The Eleventh Annu. Int. Workshop* pp 574–9

[15] Lou L *et al* 2010 Sensorized guidewires with MEMS tri-axial force sensor for minimally invasive surgical applications *IEEE Proc. of Eng. in Medicine and Biology Society (EMBC), 2010 Annu. Int. Conf.* pp 6461–4

[16] Rebello K J 2004 Applications of MEMS in surgery *Proc. IEEE* **92** 43–55

[17] Haga Y and Esashi M 2004 Biomedical microsystems for minimally invasive diagnosis and treatment *Proc. IEEE* **92** 98–114

[18] Mokwa W 2007 Medical implants based on microsystems *Meas. Sci. Technol.* **18** R47–57

[19] Wu C H, Zorman C A and Mehregany M 2006 Fabrication and testing of bulk micromachined silicon carbide piezoresistive pressure sensors for high temperature applications *IEEE Sensors J.* **6** 316–24

[20] Receveur R A M, Lindemans F W and Rooij N F de 2007 Microsystem technologies for implantable applications *J. Micromech. Microeng.* **17** R50–80

[21] Wang Q, Zhang L, Sun C and Xu Q 2008 Multiplexed fiber-optic pressure and temperature sensor system for down-hole measurement *IEEE Sensors J.* **08** 1879–83

[22] Fedder G K, Howe R T, Liu T-J K and Quevy E P 2008 Technologies for cofabricating MEMS and electronics *Proc. IEEE* **96** 306–22

[23] Tsai M-H, Sun C-M, Liu Y-C, Wang C and Fang W 2009 Design and application of a metal wet-etching post-process for the improvement of CMOS-MEMS capacitive sensors *J. Micromech. Microeng.* **19** 105017

[24] Li D, Zhao T, Yang Z and Zhang D 2010 Monolithic integration of a micromachined piezoresistive flow sensor *J. Micromech. Microeng.* **20** 035024

[25] Li D, Li T and Zhang D 2011 A monolithic piezoresistive pressure-flow sensor with integrated signal-conditioning circuit *IEEE Sensors J.* **11** 2122–8

[26] Tan S S, Liu C Y, Yeh L K, Chiu Y H and Hsu K Y J 2011 A new process for CMOS MEMS capacitive sensors with high sensitivity and thermal stability *J. Micromech. Microeng.* **21** 035005

[27] Hsieh H-S, Chang H-C, Hu C-F, Cheng C-L and Fang W 2011 A novel stress isolation guard-ring design for the improvement of a three-axis piezoresistive accelerometer *J. Micromech. Microeng.* **21** 105006

[28] Liu Y C, Tsai M-H, Tang T-L and Fang W 2011 Post-CMOS selective electroplating technique for the improvement of CMOS-MEMS accelerometers *J. Micromech. Microeng.* **21** 105005

[29] Nair P R and Alam M A 2007 Design considerations of silicon nanowire biosensors *IEEE Trans. Electron Devices* **54** 3400–8

[30] Gao Z, Agarwal A, Trigg A D, Singh N, Fang C, Tung C-H, Fan Y, Buddharaju K D and Kong J 2007 Silicon nanowire arrays for label-free detection of DNA *Anal. Chem.* **79** 3291–7

[31] Toriyama T, Tanimoto Y and Sugiyama S 2002 Single crystal silicon nano-wire piezoresistors for mechanical sensors *J. Microelectromech. Syst.* **11** 605–11

[32] He R and Yang P 2006 Giant piezoresistance effect in silicon nanowires *Nature Nanotechnology* **1** 42–6

[33] Reck K, Richter J, Hansen O and Thomsen E V 2008 Piezoresistive effect in top-down fabricated silicon nanowires *Proc. IEEE MEMS* pp 717–20

[34] Neuzil P, Wong C C and Reboud J 2010 Electrically controlled giant piezoresistance in silicon nanowires *Nano Lett.* **10** 1248–52

[35] Soon B, Neuzil P, Wong C, Reboud J, Feng H and Lee C 2010 Ultrasensitive nanowire pressure sensor makes its debut *Procedia Eng.* **5** 1127–30

[36] Singh P, Miao J, Park W-T and Kwong D-L 2011 Gate-bias-controlled sensitivity and SNR enhancement in a nanowire FET pressure sensor *J. Micromech. Microeng.* **21** 105007

[37] Kanda Y and Yasukawa A 1997 Optimum design considerations for silicon piezoresistive pressure sensors *Sensors Actuators A* **62** 539–42

[38] Gong S-C and Lee C 2001 Analytical solutions of sensitivity for pressure microsensors *IEEE Sensors J.* **1** 340–4

[39] Pramanik C and Saha H 2006 Piezoresistive pressure sensing by porous silicon membrane *IEEE Sensors J.* **6** 301–9

[40] Pramanik C, Saha H and Gangopadhyay U 2006 Design optimisation of a high performance silicon MEMS piezoresistive pressure sensor for biomedical applications *J. Micromech. Microeng.* **16** 2060–6

[41] Park S-J, Doll J C, Rastegar A J and Pruitt Beth L 2010 Piezoresistive cantilever performance-part II optimization *IEEE J. Microelectromech. Syst.* **19** 149–61

[42] Lund E and Finstada T G 2004 Design and construction of a four-point bending based set-up for measurement of piezoresistance in semiconductors *Rev. Sci. Instrum.* **75** 4960–6

[43] Henning A K, Chan N N, Watt J T and Plummer J D 1987 Substrate current at cryogenic temperatures: measurements, and a 2D model for CMOS technology *IEEE Trans. Electron Devices* **34** 64–74

[44] Kanda Y 1982 A graphical representation of the piezoresistance coefficients in silicon *IEEE Trans. Electron Devices* **29** 64–70

[45] Ziebart V, Paul O and Baltes H 1999 Strongly buckled micromachined square membranes *J. Microelectromech. Syst.* **8** 423–32

[46] Eaton W P, Bitsie F, Smith J H and Plummer D W 1999 A new analytical solution for diaphragm deflection and its application to a surface-micromachined pressure sensor *Proc. Int. Conf. on Modeling and Simulation of Microsystems, MSM 99 (San Juan, Puerto Rico, USA)*

[47] Yang J, Gaspar J and Paul O 2008 Fracture properties of LPCVD silicon nitride and thermally grown silicon oxide thin films from the load-deflection of long Si_3N_4 and SiO_2/Si_3N_4 diaphragms *J. Microelectromech. Syst.* **17** 1120–34

[48] Hatty V, Kahn H and Heuer A H 2008 Fracture toughness, fracture strength, and stress corrosion cracking of silicon dioxide thin films *J. Microelectromech. Syst.* **17** 943–7

[49] Huang H, Hu X Z, Liu Y, Bush M, Winchester K, Musca C, Dell J and Faraone L 2005 Characterization of mechanical properties of silicon nitride thin films for MEMS devices by nanoindentation *J. Mater. Sci. Technol.* **21** 13–6

[50] Bistuéa G, Elizaldea J G, García-Alonsob S, Castañoa E, Graciaa F J and García-Alonsoa A 1997 A design tool for

pressure microsensors based on FEM simulations *Sensors Actuators* A **62** 591–4

[51] Hsin C-L, Mai W, Gu Y, Gao Y, Huang C-T, Liu Y, Chen L-J and Wang Z-L 2008 Elastic properties and buckling of silicon nanowires *Adv. Mater.* **20** 3919–23